Structure of the Séchilienne unstable slope from large-scale three-dimensional electrical tomography using a Resistivity Distributed Automated System (R-DAS)

M Lajaunie, J Gance, P Nevers, J-P Malet, C. Bertrand, T Garin, G. Ferhat

Geophysical Journal International

Geophys. J. Int. (2019) **219,** 129–147
Advance Access publication 2019 June 06
GJI Marine Geosciences and Applied Geophysics

doi: 10.1093/gji/ggz259

Structure of the Séchilienne unstable slope from large-scale three-dimensional electrical tomography using a Resistivity Distributed Automated System (R-DAS)

M. Lajaunie,[1] J. Gance,[2] P. Nevers,[3] J.-P. Malet,[1,4] C. Bertrand,[3] T. Garin[3] and G. Ferhat[1,5]

[1] *Institut de Physique du Globe de Strasbourg – CNRS UMR* 7516*, EOST/University of Strasbourg, 67084 Strasbourg, France. E-mail: mlajaunie@unistra.fr*
[2] *IRIS Instruments, 45100 Orléans, France*
[3] *Laboratoire Chrono-Environnement—CNRS UMR* 6249*, THETA/University of Bourgogne Franche-Comté, 25030 Besançon, France*
[4] *Ecole et Observatoire des Sciences de la Terre—CNRS UMS* 830*, University of Strasbourg, 67084 Strasbourg, France*
[5] *INSA Strasbourg,* 67084 *Strasbourg Cedex, France*

Accepted 2019 June 5. Received 2019 May 2; in original form 2019 January 17

SUMMARY

This work presents a 3-D resistivity model of the Séchilienne unstable slope acquired with a network of portable resistivimeters in summer 2017. The instrumentation consisted in distributed measuring systems (IRIS Instruments FullWaver) to measure the spatial variations of electrical potential. 23 V-FullWaver receivers with two 50 m dipoles have been deployed over an area of circa 2 km^2; the current was injected between a fixed remote electrode and a mobile electrode grounded successively at 30 locations. The data uncertainty has been evaluated in relation to the accuracy of electrodes positioning. The software package BERT (Boundless Electrical Resistivity Tomography) is used to invert the apparent resistivity and model the complex data set providing the first 3-D resistivity model of the slope. Stability tests and synthetic tests are realized to assess the interpretability of the inverted models. The 3-D resistivity model is interpreted up to a depth of 500 m; it allows identifying resistive and conductive anomalies related to the main geological and hydrogeological structures shaping the slope. The high fracturation of the rock in the most active zone of the landslide appears as a resistive anomaly where the highest resistivity values are located close to the faults. A major drain formed by a fault in the unaltered micaschist is identified through the discharge of a perched aquifer along the conductive zone producing an important conductive anomaly contrasting with the unaltered micaschist.

Key words: Hydrogeophysics; Electrical resistivity tomography (ERT); Tomography.

1 INTRODUCTION

The Séchilienne slope is one of the largest and most active landslides of the European Alps with a volume estimated at ca. 60 ± 10 M m^3 and depths in the range of 150–200 m (Le Roux *et al.* 2011). The geology consists of fractured hard rocks (micaschists) with double permeability and strong spatial heterogeneities. The deformation of the slope is monitored by on-site extensometric gauges and at distance by a terrestrial radar and a total station since more than 20 yr (Duranthon *et al.* 2003). The hydrogeological and hydrochemical processes in the fractured hard rock (water infiltration and chemical alteration) control the deformation of the unstable slope. The complex structures of the slope (fractures, spatial variation in the degree of microfracturation, and clay deposits in the porosity) create preferential water flow paths characterized by specific geochemical signatures (Vallet *et al.* 2015). In order to constrain these flow paths and understand the hydrogeomechanical response of the slope to forcing rainfall events, and to the seasonal hydrological cycle, a better knowledge of the slope structures is needed. Images of the in-depth structures of large slopes can be obtained through geomechanical modelling if the observation of the surface displacements over time allows inferring the internal mechanical process controlling the deformation (Cappa *et al.* 2014) or by geophysical surveys. The latest can provide relevant information on the structures and discontinuities shaping the subsurface. Geophysical methods have been used in the past to study the Séchilienne slope (Duranthon & Effendiantz 2004; Meric *et al.* 2005; Jongmans and Garambois 2007; Helmstetter & Garambois 2010; Le Roux *et al.* 2011). Imaging the variations in the electrical properties of the Séchilienne slope has proven to be insightful for understanding the subsurface geological and hydrological properties and delineating zones with specific mechanical behaviours (Meric *et al.* 2005; Le Roux *et al.* 2011). However, these surveys were based on profile measurements and 2-D assumptions were made, considering that the subsurface

is homogeneous laterally to the profiles. This assumption allows a first-order interpretation of the data, but artefacts are locally produced by the strong gradient of the topography (locally close to 45°) perpendicular to the survey line and the presence of 3-D structures.

At Séchilienne, imaging complex structures at a few hundreds of metres below the surface necessitates the application of 3-D electrical surveys. Such type of investigation is rarely applied to landslides because of rough topographies, presence of vegetation, and, in general, difficult access to the measurement sites. Moreover, large depths of investigation require large spacing between injection electrodes and therefore the spreading of several kilometres of heavy multicore cables for standard measurements with multi-electrodes resistivity meters. Most of the landslide 3-D models presented in the literature were created from the interpolation of multiple 2-D profiles (Travelletti and Malet 2012; Gance *et al.* 2015). Only a few examples exist where 'real' 3-D landslide surveys have been carried out but these investigations were limited to small depths of investigation (from 10 to 30 m: Friedel *et al.* 2006; Uhlemann *et al.* 2017). This study takes advantage of recently developed Resistivity Distributed Automated Systems (R-DAS) for electrical resistivity measurements. R-DAS are easily portable and heavy cable free systems that allow overcoming the previously mentioned difficulties. 3-D electrical data acquired over a large-scale array (1.5 km^2) using the FullWaver system from IRIS Instruments are presented and interpreted. The DC resistivity data set is processed and inverted with the BERT software package (Günther *et al.* 2006; Rücker *et al.* 2006). A resistivity model is proposed and interpreted taking into consideration the previous geotechnical, geophysical and hydrogeological studies. The objectives of the work are (1) to propose a 3-D resistivity model of the Séchilienne slope up to a depth of 500 m, (2) to discuss the quality of data and of the inversion models and (3) to interpret the 3-D resistivity model in terms of rock properties, structure and microstructure and water content. In particular, the impacts of the sparseness and quality of the resistivity measurements are discussed. Sensitivity tests are carried out to define the limits of interpretability of the models.

2 EXPERIMENTAL SITE: THE SÉCHILIENNE LANDSLIDE

2.1 Geological and geomorphological setting

The Séchilienne slope is located on the right bank of the Romanche River, South East of Grenoble (Isère, France). From a geological viewpoint, the slope is part of the Palaeozoic external crystalline massif of Belledonne. The substratum is mainly composed of micaschists characterized by an N-S trending subvertical foliation. Stratigraphically discordant carbonate deposits from the Carbonifer to the Lias eras cover micaschists located on the top East of the massif (Mont Sec) and along the massif ridge line. The slope is also locally covered by Quaternary (Würm) glacio-fluvial deposits (Vengeon 1998; Vallet *et al.* 2016). The volume of the unstable slope is estimated to 60 M m^3 (Le Roux *et al.* 2011). The most active part of the landslide, named 'Les Ruines', is located on the eastern border of the unstable zone. Its volume is estimated at 3 M m^3. The measured surface velocity is in the range of 10 cm yr^{-1} for most of the unstable slope to nearly 300 cm yr^{-1} in the active part (Dubois *et al.* 2014). The landslide extends from 400 to 1100 m elevation (Le Roux *et al.* 2011) and presents steep slopes around 35°–40° resulting from the incision by the Romanche River and the ice of the Romanche glacier during the Quaternary glaciations (Montjuvent and Winistorfer 1980). Above 1100 m, a major head scarp about 10 m high and several hundreds of metres wide separates the Mont Sec from the northern part of the unstable zone. The morphology of the Mont Sec corresponds to a glacial plateau with local moraine deposits mixing amphibolite and gneiss clasts. To the north, the presence of peat filling locally north–south depressions with a maximum thickness of 10 m has been noticed by Legchenko *et al.* (2011). To the east, a north-South fault scarp delineates the landslide boundaries. To the west and the south, no clear geomorphological evidence of landslide activity is identified. In depth, the landslide is characterized by a deep progressive deformation with a maximum depth estimated at 150 m (Le Roux *et al.* 2011) which is hard to estimate due to the absence of a well-defined basal sliding surface. The geological information (identification of the faults at the surface and in the anthropogenic gallery of Electricité de France–EDF—at the base of the slope, interpretation of 2-D resistivity and seismic profiles) have been summarized by Baudement *et al.* (2013) and integrated in a Gocad-derived 3-D model used for the interpretation of the 3-D resistivity model.

Two boreholes (SC1, SC2; Fig. 1c) were drilled in 2010 in the unstable area at depths up to 150 m. Analysis of the core samples provide direct information on the lithology and fracturation of the slope. The micaschists present very local variations in the nature of the fillings (clay, calcite, sandstone, iron oxide, chlorite, quartz veins and pyrite) and in the tectonic and geochemical processes (fracturation, alteration and oxidation). Very fractured sections are observed at several depths; these sections are characterized locally by a total loss of continuity in the cores. The two boreholes do not present the same sequence of lithology and fracturation demonstrating the heterogeneity of the slope induced by the gravitational deformation.

Inclinometer observations have been acquired at least once a year in SC1 and SC2 from 2009 to 2014 (Fig. 1c). At SC1, the vertical profile of velocity identifies two units separated by deformation surfaces at *ca.* −60 and −106 m; at SC2, only one deformation surface at *ca.* −112 m is observed. The depth of the instability can thus be considered in the range of around −110 m (Duranthon 2013).

2.2 Hydrogeological setting

The heterogeneity in fracturation and microstructure controls the location of the flow paths and the transit times (Vallet *et al.* 2015). The Mont-Sec massif is characterized by a dual-permeability behaviour typical of fractured rocky aquifers where permeable fractures play a major role in the drainage. High flow velocities (ranging from 0.45 to 0.84 km d^{-1}) are observed in the Sabot fractures and in the Séchilienne fault system) and low flow velocities (0.08 km d^{-1}) are observed in the less pervious microfracturation bypassing the main fractures (Mudry and Etievant 2007). At the base of the slope, the EDF gallery (Fig. 1a) acts as a major drain of the massif (Vallet *et al.* 2015).

The difference in hydraulic conductivity between the unstable zone (very fractured) and the underlying stable bedrock creates a system of two-layer aquifer with a shallow perched aquifer, localized in the unstable zone and a deep aquifer connected by major fractures. The landslide perched aquifer is temporarily and mainly discontinuous and its extent and connectivity fluctuate according to short-term recharge events through a dense network of open fractures associated to trenches and counterscarps at the surface. During the high-flow periods, a water input from the top sedimentary cover

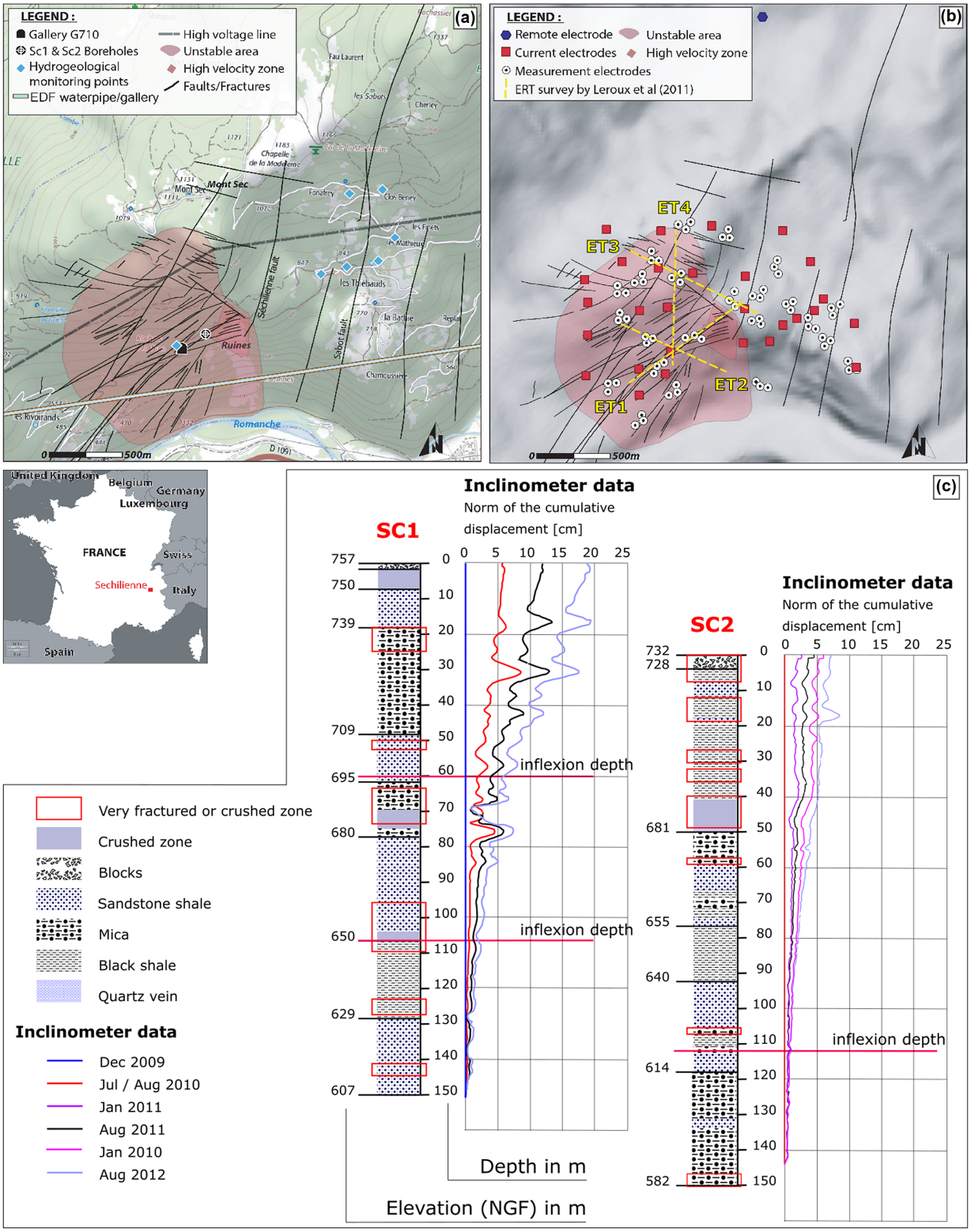

Figure 1. Morphology of the Séchilienne slope: (a) geomorphological setting (fault model from Barféty *et al.* 1972 and Vengeon 1998—appendices I and II) and location of boreholes and water sampling points. (b) Location of the portable Full-Waver resistivity measurements and of the 2-D ERT profiles acquired by Le Roux *et al.* (2011). (c) Lithological profile of the unstable slope obtained from core samples from the SC1 and SC2 boreholes, related time-lapse inclinometer observations and their respective interpretation (Duranthon 2013).

close to Mont Sec also contributes to the recharge, while during the low-flow periods, the perched aquifer is almost dry (Guglielmi *et al.* 2002; Vallet *et al.* 2015). The hydraulic behaviour is very contrasted between high- and low-flow periods (Vallet *et al.* 2015). During high-flow periods, the recharge amount is sufficient to maintain the perched aquifer saturated and the numerous disconnected saturated zones are temporarily connected (Cappa *et al.* 2014). A subsurface drainage of the perched aquifer occurs in these periods, mostly controlled by fractures oriented at N70. During the low-flow periods, temporarily disconnected saturated zones appear. These disconnected zones are filled after rain events but are not sustained because of the low recharge amount. The deep aquifer, which extends all over the massif, corresponds to a deep saturated zone (altitude around 550 m asl) in the fractured bedrock; the vadose zone above it is about 100 m thick (Vallet *et al.* 2015).

2.3 Landslide kinematics

Changes in landslide displacement rates are controlled by rainfall events as identified by the positive correlation between antecedent cumulative precipitation and average velocities (Rochet *et al.* 1994; Alfonsi 1997). Vallet *et al.* (2016) identified a correlation between the water recharge (instead of the precipitation) and the surface displacement rates. Recharge variations and surface displacement rates are seasonally linked with high displacement rates during high-flow periods and low displacement rates during low-flow periods (Vallet *et al.* 2016). Moreover, as hypothesized by Cappa *et al.* (2014), high water pressures in the deep aquifer can facilitate the rupture of the landslide due to stress transfer and frictional weakening during groundwater-level changes. So far, these results are based on few punctual surface observations and remain difficult to spatialize, particularly at depth. In this context, the imaging of the 3-D spatial variations of the electrical resistivity could be useful to confirm and enrich the previous results.

3 GEOPHYSICAL INSTRUMENTATION AND DATA

To image the structure of the slope up to a depth of 500 m, a 3-D resistivity tomography with an array of portable electrical automated resistivimeters has been carried out in 2017 July over an area of 2.0 km^2 (Fig. 1b).

3.1 Resistivity-DAS: electrical measurement devices and acquisition setup

The FullWaver system of IRIS Instruments is composed of several autonomous receivers (V-FullWaver) and of one autonomous current recorder (I-FullWaver) connected to a 3 kW high-power transmitter (TIPIX—IRIS Instruments). The combination of the receivers and the transmitter forms an R-DAS. The measurement principle of the Fullwaver system is the same than the one used for multi-electrode resistivimeters (Fig. 2). It consists in measuring the current injected by the transmitter between two current electrodes and the resulting voltage between two reception electrodes. The differences with multi-electrode systems are that:

(1) The transmitter and receiver systems are separated (instead of being in one box) to avoid electromagnetic interference of strong power transmitted to the receiver.

(2) The receiver system is composed of multiple autonomous receivers connected to a maximum of three electrodes. With this technology, the receivers are not linked together by any cable allowing the planning of 3-D electrical surveys on rough topography.

(3) The transmitter and receivers are separated, so, instead of being synchronized to the same internal clock, the measurements are time stamped to the Global Navigation Satellite System (GNSS) clock.

(4) The current and voltage are recorded as time-series with a sampling frequency of 100 Hz, requiring to process the data afterwards with advanced signal processing techniques.

At Séchilienne, 23 V-FullWavers connected to three electrodes were used, forming two 50 m orthogonal dipoles, constituting a measurement network of 69 electrodes. The theoretical positioning of the electrodes was planned using orthophotographs in order to distribute the systems as regularly as possible, taking into account the rough topography and the accessibility to the measurement sites. In practice, on site, the positioning was slightly adapted. The survey was realized over five days in 2017 July in a period of high-water flows at the end of the Spring season. On site, each day, the V-FullWavers were programmed in the morning and recordings were acquired during the whole day. At the end of the day, the V-FullWavers were taken back for data collection and recharge of the battery. The current injections have been realized between a fixed remote electrode located at 1.5 km north from the investigation area, at an altitude of 1079 m (asl) and a mobile current electrode successively grounded at 30 locations distributed over the studied area (Fig. 1b), at various altitudes between 51 m above and 535 m below the fixed remote electrode. The fixed remote electrode (Fig. 3d) was buried in a forested area in a trench filled with salted water. The injection cable was set as far as possible from the reception cable in order to limit inductive and capacitive coupling effects. A great attention was paid to lower the contact resistance at the mobile current electrode (by adding 20 L of salted water) five minutes before each injection and at the remote electrode (by adding 40 L of salted water each day). The contact resistance measured between the injection and remote electrodes was in the range 0.4–4.0 kΩ, allowing injecting a current between 0.5 and 3.2 amp. The total injection time was at least of 400 s corresponding to 100 stacks for 2 s injection duration. This duration has been increased up to 600s (150 stacks) for the lower amperages (Fig. 6c). At the measurement electrodes, it was not possible to add water every day because of the sharp topography and the difficult accessibility. As a consequence, the contact resistance can be relatively high with mean contact resistance of 15 kΩ and a maximum of 67 kΩ (Fig. 6b). This range of contact resistance is however not affecting the measurements because of the high input impedance of the FullWaver systems (100 MΩ). The position of each electrode was measured by differential GNSS using Trimble R8s receivers; the GNSS data set was processed with the TBC (Trimble Business Centre) software. A permanent GNSS antenna belonging to the French geodetic datum (RGF93) was used to cluster the measurements to the national topographic reference. In order to achieve the best position determination, two base stations were used at close distance (1.2 km) from the site. The use of two base stations allows estimating accuracy on each position, in the range from 0.02 to 0.60 m in the horizontal plane. The lowest accuracy corresponds to measurement points located under forest vegetation.

3.2 Data quality control

Data were measured with a good quality for the first four days of measurements. The fifth day, the measurements were realized

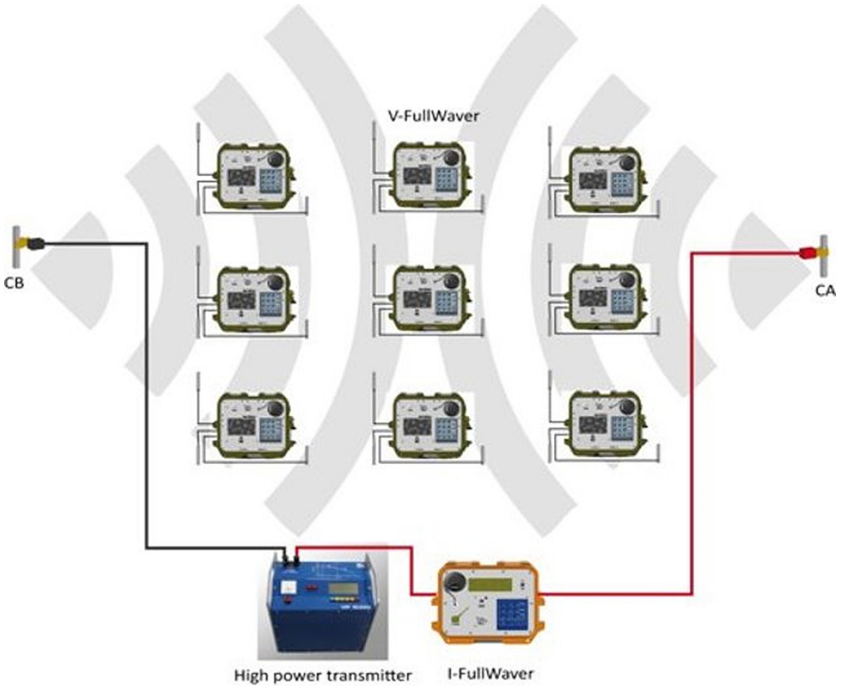

Figure 2. Principle of measurement of the FullWaver system. The measurements electrodes (connected to the V-FullWaver) are fixed at one location and record the current potential during the survey. The current injection electrodes (connected to the I-FullWaver) are moved. For the Séchilienne experiment, CA is fixed and located at a remote distance of 1.5 km from the investigation area.

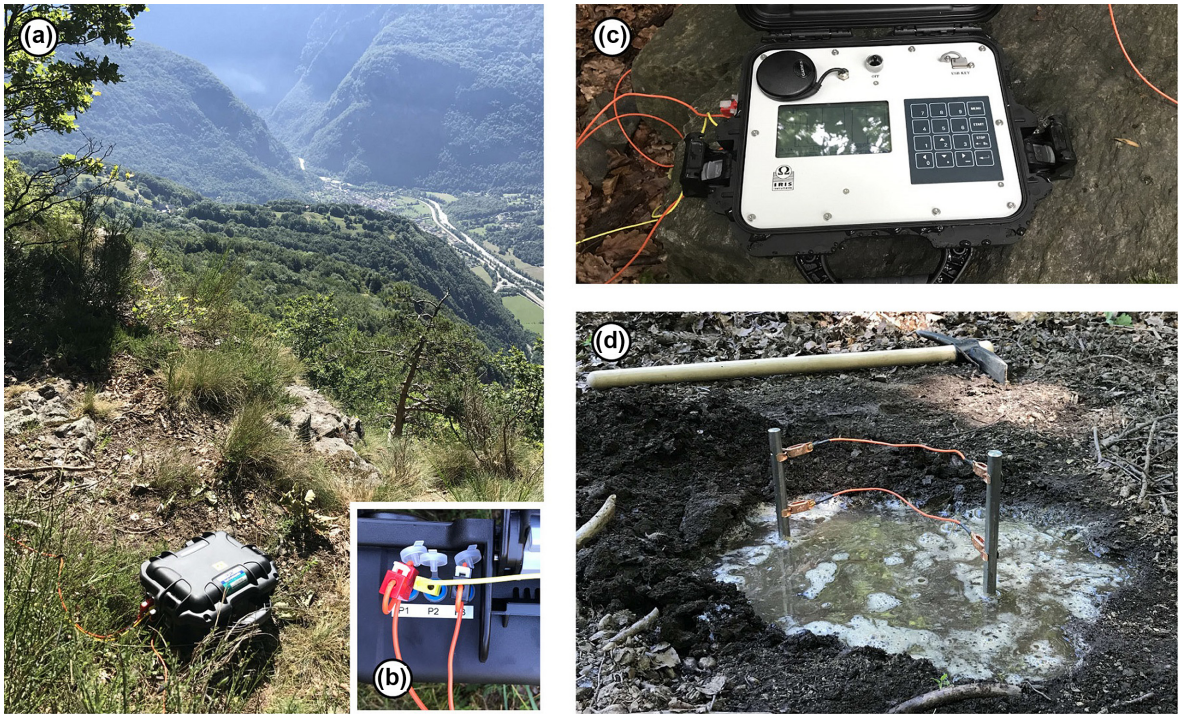

Figure 3. Photographs of the monitoring equipment and of the measurement sites: (a) V-FullWaver unit at position FW9. (b) Zoom on the plugs for the three measurement channels on a V-FullWaver unit. (c) Zoom on the control screen of a V-FullWaver unit. (d) Remote electrode fully watered with a highly conductive salted mixture.

while a thunderstorm was approaching. This is clearly visible on the voltage measurements of this day showing a lot of spikes and a charging of the soil with a sudden increase of the self-potential (Fig. 4). All measurements were stopped when the thunder hit the mountain and started again some hours later.

4 METHODOLOGY

The methodology to create a resistivity model of the slope consists in (1) the extraction and pre-processing of the raw data, (2) the filtering and error assessment of the data, (3) the test of inversion parameters,

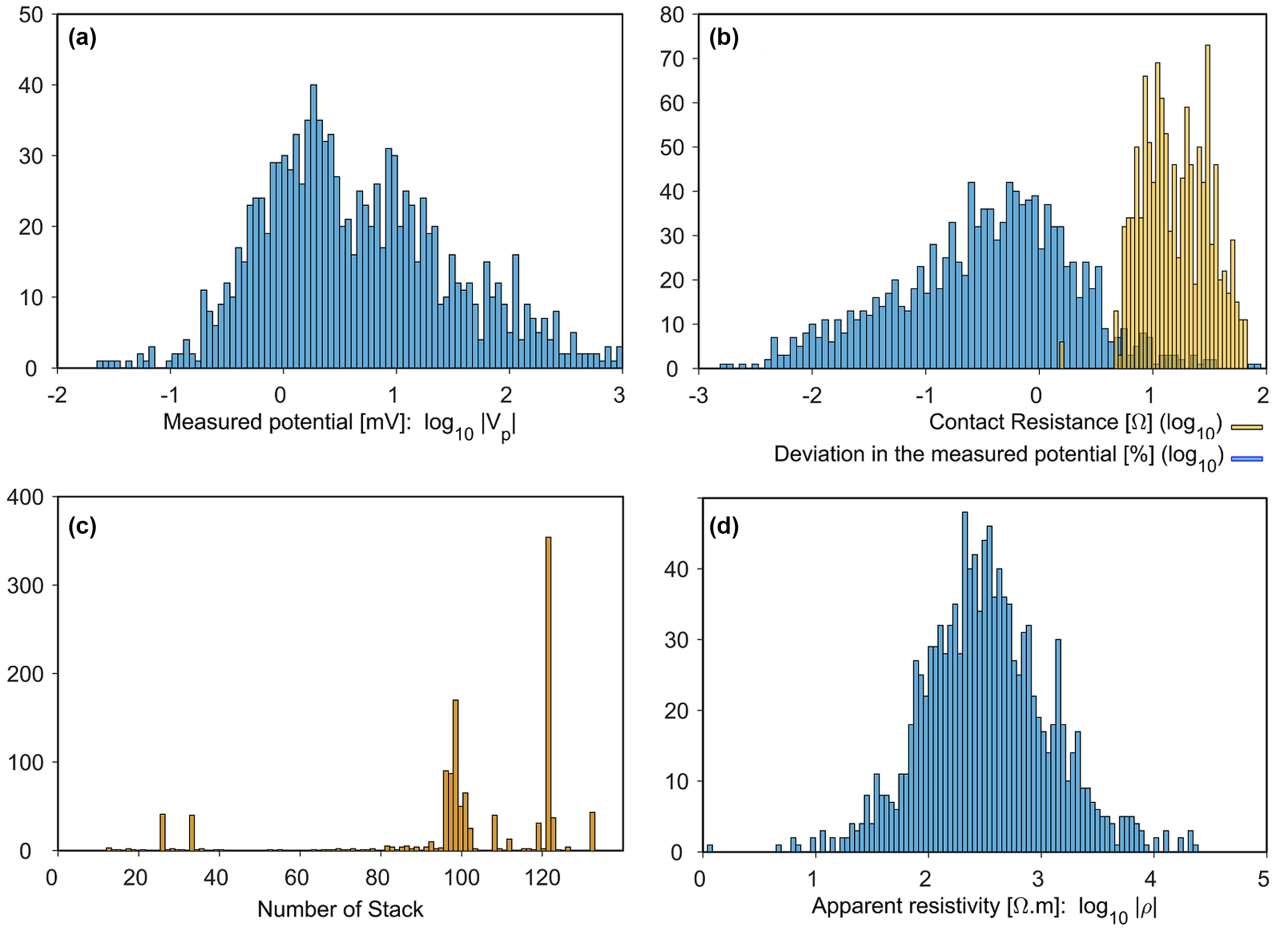

Figure 4. Distribution of voltage observations: (a) distribution of the measured electric potential (in mV). (b) Distribution of contact resistance values and deviation in the measured potential. (c) Distribution of the number of stack for each data and (d) distribution of the apparent resistivity values.

and (4) the sensitivity analysis of the model parameters. The four steps are presented in Fig. 5. The software FullWave Viewer is used for pre-processing the data (step 1), and the software package BERT (Günther *et al.* 2006; Rücker *et al.* 2006) is used for the inversion and sensitivity tests (steps 3 and 4).

4.1 Data extraction and pre-processing

The voltage data of all electrodes were processed with the IRIS Instruments software FullWave Viewer (Fig. 4). The processing consists in resynchronizing possible unsynchronized time-series, filtering spikes and self-potential jumps, stacking the different periods after synchronous detection of the fronts, computing the average voltage over a part of the injection window on the stacked period, computing the average current over a part of the injection window on the stacked period, calculating the resistance from the previous measurements, calculating the chargeability over 20 windows during the off-time of the stacked period, and finally calculating the total chargeability from the 20 windows and the associated standard deviations. The data with low signal (typically Vp < 0.1 mV) and high standard deviations (typically std $>$ 200 mV V^{-1} or 20 per cent) have been reprocessed manually. The measured chargeability is comprised in the range from 10 to 30 mV V^{-1}. This high chargeability is explained by the presence of disseminated pyrite.

4.2 Data filtering

4.2.1 Extreme topographic effects

The roughness of the slope, the presence of high slope gradients and of sharp topographic anomalies (scarps, depressions) are impacting the computation of the apparent resistivity inducing anomalies; this is referred as the topographic effect t (Fox *et al.* 1980; Rücker *et al.* 2006). The topographic effect t is the ratio between the approximated geometric factor for a homogeneous half-space k_a and the true geometric factor k according to eq. (1):

$$t = \frac{k_a}{k} \tag{1}$$

A high-resolution digital surface model (DSM), acquired from an airborne LIDAR (LIght Detection And Ranging) survey (0.5 m spatial resolution) over the landslide and complemented with a lower resolution DSM (5 m) acquired by airborne stereo-photogrammetry over the surrounding stable slopes are combined to obtain a realistic topography of the slope. Using the resulting DSM, sampled at a spatial resolution of 0.2 m, the t-value is computed by means of forward computation (Rücker *et al.* 2006), providing a distribution of t-values (Fig. 7a). In this study, the survey layout and the topographic variations lead to topographic effects ranging from -90 to 12 . A few data display extremal topographic effect (less than -4

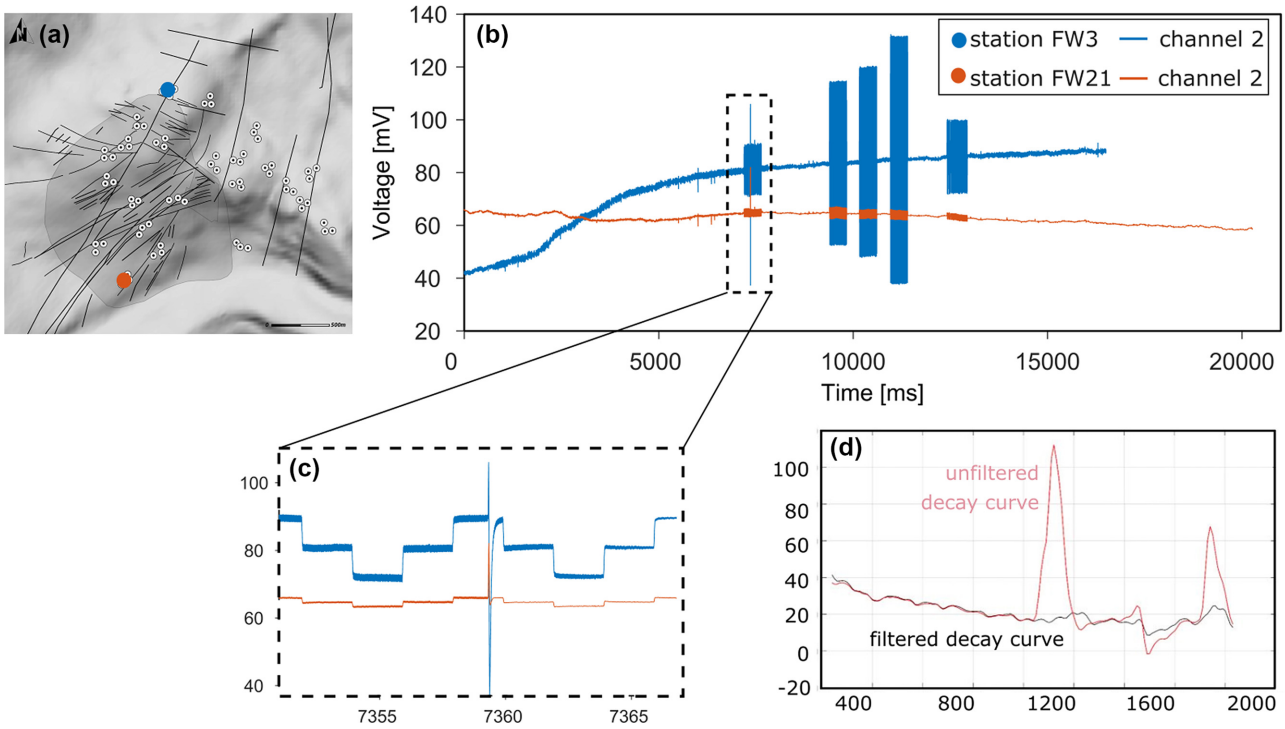

Figure 5. Example of raw voltage time series and impact of spike noise filtering: (a) location of the stations FW3 and FW21 at the top and base of the investigated area. (b) Example of one day of measurement at stations FW3 and FW21 (data from the second day of measurements). (c) Example of spikes in the measured voltages recorded during a thunderstorm. (d) Effect of spike noise filtering on the decay curve: the unfiltered decay curve in red displays some spikes, efficiently filtered by the despiking procedure (black curve).

or more than +6) (Fig. 7a). These data correspond mostly to situation where the geometrical factor is extremal (higher than 10^6 in absolute value, Fig. 7b), therefore associated to very low potential measurements at the receivers. The associated data points—affected by a very high uncertainty—have been removed. Over 1181 data arising from the pre-processing, 14 data have been filtered because of extreme topographic effect, and 19 additional data have been filtered during the inversion because of high uncertainty. In total, 1148 data are introduced in the inversion process.

4.2.2 *Effect of electrode layout on data uncertainty*

Because of the unusual geometrical layout of the survey (i.e. the measurement dipoles are very small in comparison to the distance between the injection electrodes and the measurement electrodes, and the injection and measurement dipoles are rarely collinear), the uncertainty associated to the electrode positioning is a possible source of errors (Uhlemann *et al.* 2015). This uncertainty propagates in the computation of the geometrical factor k, and can be highly amplified locally for specific cases of unusual (not aligned) quadrupolar geometries. In particular, when considering quadrupoles formed by two orthogonal dipoles, one in the alignment of the other, such that the two measurement electrodes are almost equidistant from each injection electrodes, the geometrical factor of such a quadrupole is exceptionally large, and low positioning errors (up to 50 cm) cause dramatic errors in the estimation of k. Two options are available. The first one is to filter out these points. The second is to compute and use their associated uncertainty in the inversion. We chose the second option as it will damp automatically and gradually each data point weight in the inversion instead of rejecting a number of data points based on a threshold value chosen subjectively. The effect of the electrode positioning on the geometrical factor has been quantified for each quadrupole using the positioning accuracy provided by the GNSS measurements (when available) or using a constant uncertainty of 2 m around the electrode when no GNSS accuracy was available. Assuming that the topographic effect is accurately computed with BERT, the error on the geometric factor can be calculated as the error on the approximated geometric factor for a homogeneous half-space . The relative error affecting the geometrical factor is calculated with eqs (2) and (3):

$$\delta k = \sum_{i,j} [\delta X_{i,j} \frac{\partial k}{\partial X_{i,j}}] \tag{2}$$

where X is successively each of the two horizontal coordinates for all four electrodes forming the quadrupole for which k is computed. In the sum, i is successively $[A, B, M, N]$ and $j = 1, 2$ scans the two horizontal coordinates, with, for example

$$\frac{\partial k}{\partial x_A} = \frac{k^2}{2\pi} \left[\frac{x_A - x_M}{[(x_A - x_M)^2 + (y_A - y_M)^2]^{3/2}} - \frac{x_A - x_N}{[(x_A - x_N)^2 + (y_A - y_N)^2]^{3/2}} \right] \tag{3}$$

The derivatives with respect to the y component and to the other electrodes have similar forms. A second uncertainty arose from the accuracy of the potential measurement itself. Following Günther *et al.* (2006), we define this error as the sum of a fixed percentage per cent p and a relative voltage error $\frac{\delta V}{V}$. The total error is expressed in eq. (4):

$$\frac{\delta \rho}{\rho} = \text{per cent } p + \frac{\delta V}{V} + \frac{\delta k}{k} \tag{4}$$

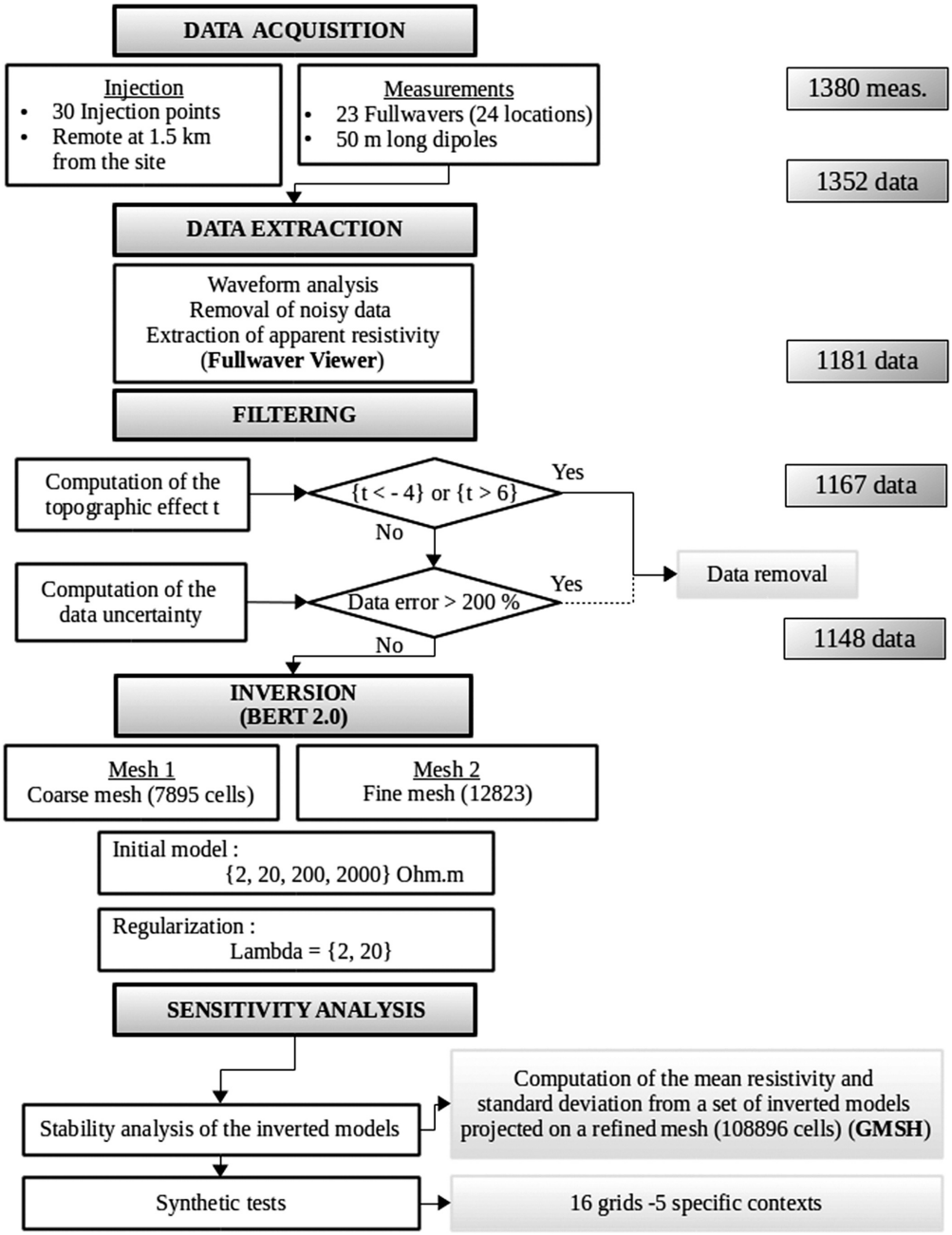

Figure 6. Methodological flowchart.

The errors are computed using a percentage error of 1 per cent and a voltage error δV of 2×10^{-5} V. Data with uncertainties higher than 200 per cent are filtered during the inversion (Fig. 7c).

4.3 Inversion strategy

Sixteen inversions of the full data set (Table 1) have been realized with the software package BERT (Rücker *et al.* 2006; Günther *et al.* 2006). BERT is based on preconditioned conjugate gradient methods. The modelling process is realized using two meshes for the computation of the primary and secondary resistivity fields and the computation of the potential is performed with quadratic shape functions. Computations are carried out on unstructured tetrahedral meshes of {340 x 340 x 200} km^3 for the forward modelling and {2 x 2.7 x 2} km^3 for the inversion (parameter mesh). The parameter mesh covers the entire survey area, including the remote (fixed) injection electrode, and its top interface describes the true topography all over and outside the covered area. Although optimal for the dimensions of the large-scale geological and hydrogeological features of the slope, the spatially sparse and irregular sampling leads to a local lack of resolution close to the surface because of the large interdistance between the FullWaver systems (between 50 and 200 m). In order to test the stability of the inversion process and to assess the areas unresolved by the data inversion, several parametrizations

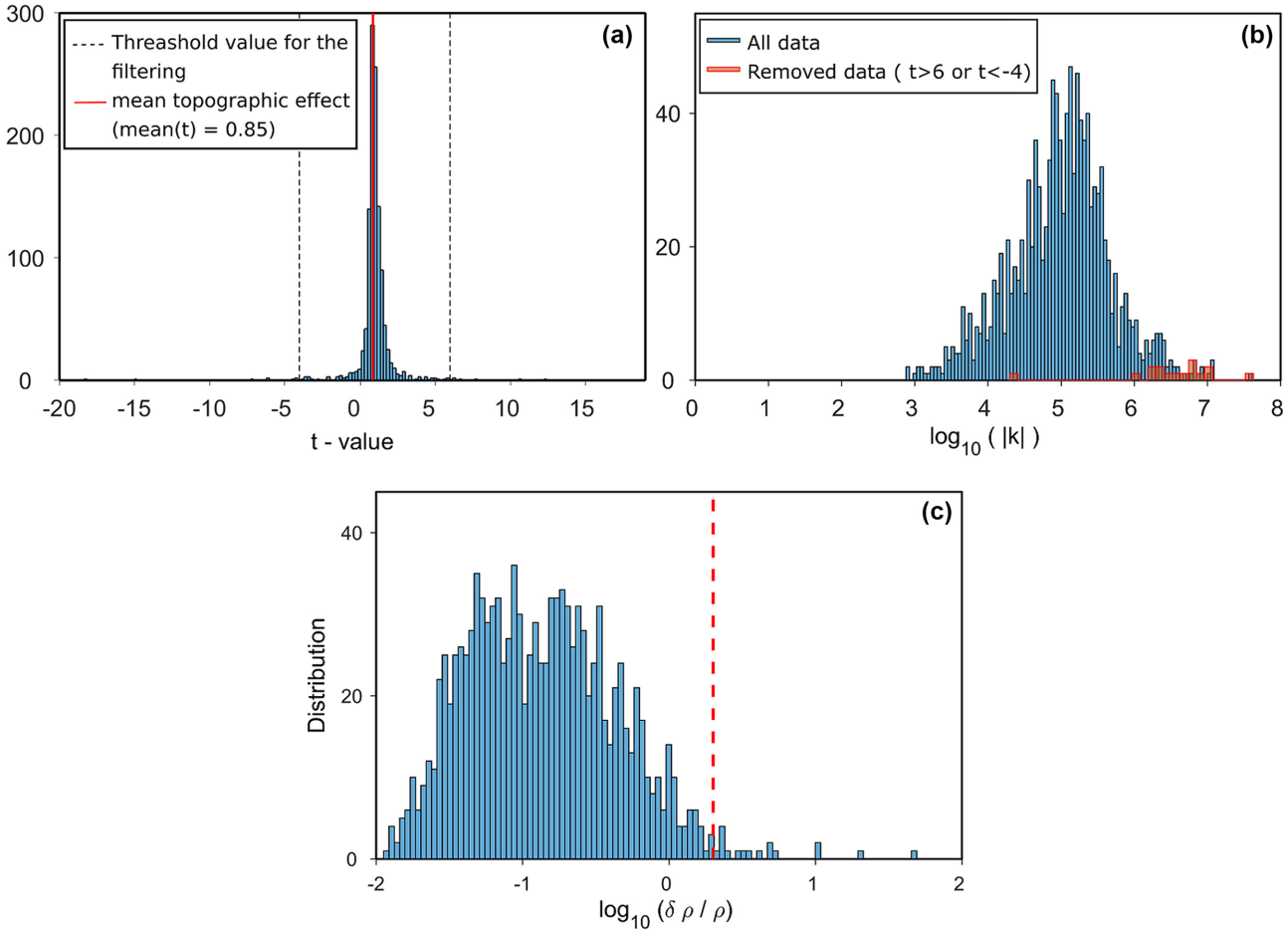

Figure 7. Data filtering: (a) distribution of topographic effects and filtering of extreme values ($t > 6$ and $t < -4$). (b) Distribution of geometrical factors (in red: geometrical factors of the data presenting extreme values of topographic effects): extreme topographic effect is often related to high geometrical factor. (c) Distribution of relative error on the apparent resistivity values.

Table 1. Values of parameters used in the inversion models.

Regularization	Initial model (homogeneous resistivity in Ω m)	Mesh
LAMBDA = 2	STARTMODEL = 2	Coarse: 7895 cells
LAMBDA = 20	STARTMODEL = 20	Fine: 12823 cells
	STARTMODEL = 200	
	STARTMODEL = 2000	

of the inversion have been tested. Sixteen inversions have been realized changing one by one three parameters controlling the inversion process:

(1) First, the regularization of the inversion, controlled in BERT by the parameter LAMBDA, defines the degree of spatial variation authorized by the inversion, hence the smoothness of the model. A weak regularization (here fixed at LAMBDA = 2) will integrate the data noise in the inverted model, while a strong regularization will prevent from inversion-induced noise but can also impeach the finest information content of the data to be expressed in the inverted model.

(2) Second, the initial model is considered homogeneous, with different resistivity values, allowing testing several areas of the model space. If the initial model is too far from the true model, the inversion might not succeed in updating the model to bring it closer to the true model. Moreover, if the data sensitivity is locally low (due to the sparse sampling), depending on the regularization, the inverted model might locally be mostly driven by the initial model. The variation in the initial model is therefore expected to allow detecting locally unresolved areas in the model.

(3) Last, the coarseness of the mesh plays a role in the quality of the modelling and in the computation of synthetic data. Coarse and fine meshes (Table 1) have been used in the inversions, for the purpose of detecting if differences arise regarding the accuracy of the modelling, given that a coarser model will necessarily provide a less accurate description of the topography.

From the sixteen inversions presented in Table 1, all 12 stable inversions (i.e. converging with reasonable misfit values and presenting stable distribution of resistivity) are selected (Section 5.1, Fig. 8). The mean and standard deviation of the logarithmic resistivity in the set of inverted models are computed on a refined mesh (108 896 cells), on which each inverted model is projected. In the following, the resulting models are respectively referred to as 'mean resistivity model' and 'standard deviation model' (Section 5.2, Fig. 9). The local dispersion of resistivity values amongst all inverted models provides information on the sensitivity: only areas displaying similar resistivity values are considered resolved by the inversion, and the sensitivity can be inferred from the discrepancy in the set of inverted models. The stack of the inverted models is used to filter noise created by the inversion. Inversion results and interpretation will be presented and discussed in Section 5, taking into account the sensitivity tests performed in the following section.

4.4 Sensitivity tests

The sensitivity of the data and of the inversion is assessed with synthetic tests (Fig. 10). Sixteen grids have been created and the synthetic data related to our survey have been computed with BERT, with respect to the resistivity values indicated in Table 2. The synthetic data have been inverted with both a strong (LAMBDA = 20) and a weak (LAMBDA = 2) regularization, using an error model computed with a similar strategy as for the field data, and expressed by eq. (4). The mean and standard deviation models of the strongly and weakly regularized models are computed for all 16 tests. The accuracy in the location, the shape and the resistivity value of the main anomalies observed in the field inverted models are tested, as well as the possible spreading induced by the inversion process. The field inverted models display resistivity values ranging from 100 to 10000 Ω m, and present the following characteristics: (1) a deep conductive anomaly located at the east of the unstable zone, extending locally towards the surface and (2) a strong resistive anomaly at the surface, all over the unstable zone at the west of the model (Sections 5.1 and 5.2, Figs 10, 11 and 13).

4.4.1 Sensitivity of the model to a conductive anomaly

The synthetic tests 1–5 (Table 2) aim at simulating a finite-dimension conductive anomaly at depth, located at the east of the unstable zone. A conductive cube has been introduced in a homogeneous material, affected by the topography of the slope. The objectives of the synthetic tests are (1) to define if conductive anomalies can be detected and accurately localized in the inverted models given the sharp topography, (2) to test if artefacts such as a spreading of the anomalous resistivity towards the surface are provoked by the inversion, (3) to estimate if the bottom of the anomaly is well determined and (4) to quantify if the resistivity values are well assessed. Results indicate that:

(1) the anomaly has to be large (of at least 200 m^3 at an altitude of 550 m) in order to be detected (the anomaly is always detected except in test 3, where the anomalous body is a cube with side length of 200 m);

(2) if it is close enough from the surface, a cubic conductive anomaly tends to spread through inversion towards the surface (a spreading is observed for tests 1 and 2 but not for tests 4 and 5). The resistivity of the spreading shape contrasts however less than the true anomaly with the background resistivity;

(3) the anomalous conductivity seems always largely underestimated, over one order of magnitude;

(4) the spatial location is accurate and the size (especially the limits at depth) is well constrained.

4.4.2 Sensitivity of the model to conductive bodies of various sizes below the Western resistive anomaly

The very damaged rocks in the unstable zone is expected to produce a very high resistivity (Le Roux *et al.* 2011). The transition to the stable zone is expected to result in a decrease of the resistivity with depth. The sensitivity to an abrupt change in resistivity is evaluated with the synthetic tests, as well as the sensitivity to variation of resistivity within this deep conductive body. The detectability of small-sized conductive anomalies located close to the surface and in the resistive sector of Mont Sec is also tested.

(1) First, a conductive anomaly in a resistive background, located at an altitude around 800 m is simulated at the location where a transition from the resistive anomaly towards a more conductive medium is expected. Four tests are realized, changing the dimensions and the location of the conductive body (Table 2; tests 6–9). An anomaly is observed in the inverted models, at the 'true' location, but with a wrong estimation of the resistivity, which is often overevaluated (particularly with strong regularization) and inside this anomaly, a gradient towards the 'true' resistivity value appears as an artefact. These anomalies are only detected below the area covered by the sensors. At depth, the limit of the anomaly is always detected.

(2) Second, anomalies of small sizes (< 200 m^3) located close to the surface are simulated above and in addition to the conductive anomaly simulated in test 9 (Table 2; tests 10 to 12). These tests indicate that such small bodies, even close to the surface, cannot be detected by the inversion.

(3) Third, a conductive anomaly, shaped as a vertical parallelepiped and oriented east–west, is included in the conductive anomaly simulated in test 9 (Table 2; test 13). Results indicate that such anomaly cannot be distinguished from the patterns obtained in test 13: a conductive anomaly is detected inside the conductive body, with wrong estimations of the resistivity values. Such pattern can thus not be detected with our measurement layout.

4.4.3 Sensitivity of the model to extreme resistive anomalies corresponding to faults

Tests were further performed to assess the detectability of vertical resistive anomalies in the Western sector of the model. The context is the presence of vertical faults crossing the unstable slope. Vertical parallelepipeds of variable thicknesses have been incorporated in the grids with high resistive values (Table 2; tests 14–16). The simulations indicate that such anomalies can be detected, for all tested thicknesses (50, 100 and 200 m). At depth, the detection is limited, and the resistivity decreases at the location of the anomaly. For anomalies of 200 m thick, the modelled resistivity value is retrieved, but for thinner anomalies, the resistivity of the anomaly is largely underevaluated. In all three cases, artefacts arise locally at the surface of the inverted model.

Table 2. Synthetic tests: location, dimensions, context and resistivity values of the simulated anomalies.

Test ID	Background resistivity [Ω m]	Anomalous resistivity [Ω m]	Altitude of the anomaly (m)	Dimension of the anomaly (E x N x Z)	Context
Test 1	500	50	550	400	Eastern conductive anomaly
Test 2	500	5	550	400	Eastern conductive anomaly
Test 3	500	5	550	200	Eastern conductive anomaly
Test 4	500	5	300	400	Eastern conductive anomaly
Test 5	500	50	300	400	Eastern conductive anomaly
Test 6	1500	300	690	800 x 1000 x 200	West. resistive anomaly
Test 7	1500	300	490	800 x 1000 x 600	West. resistive anomaly
Test 8	1500	300	690	1000 x 1400 x 200	West. resistive anomaly
Test 9	1500	300	490	1000 x 1400 x 600	West. resistive anomaly
Test 10	1500	300	300	1000 x 1400 x 500	West. resistive anomaly
		300	800	200 x 200 x 50	West. resistive anomaly
Test 11	1500	300	300	1000 x 1400 x 500	West. resistive anomaly
		300	885	100 x 100 x 50	West. resistive anomaly
Test 12	1500	300	300	1000 x 1400 x 500	West. resistive anomaly
		300	900	100 x 100 x 20	West. resistive anomaly
Test 13	1500	300	300	1000 x 1400 x 500	Conductive fault
		50	300	1000 x 200 x 500	Conductive fault
Test 14	800	2000	390	200 x 1000 x 800	Resistive fault
Test 15	800	2000	390	100 x 1000 x 800	Resistive fault
Test 16	800	2000	390	50 x 1000 x 800	Resistive fault

5 GEOPHYSICAL MODELLING: QUALITY OF THE INVERSION MODELS

5.1 Inversion results

The 16 inversions (Section 4.3, Table 2) converged with reasonable χ^2 values ($0.88 < \chi^2 < 1$). The distribution of the resistivity values for all inverted models are presented in Figs 9(a) and (e). The distributions of resistivity values are stable within the group of inverted models produced by a same regularization parameter when considering only inversion with initial models of 2, 20 and 200 Ω m. The inversions with initial model of 2000 Ω m produces models with higher resistivity values indicating that the initial model constrains largely the inversion process. Therefore, only the inverted models with initial models of 2, 20, and 200 Ω m are further considered in the analysis. From the three tested parameters controlling partly the inversion, it seems that the parameter influencing the most the resistivity model is the regularization parameter.

Two models are presented as examples for the two regularizations are presented in Figs 9(b)–(d), and (f)–(h). A weak regularization provides a patchy aspect at the surface (Fig. 9f), partly resulting from the inversion process, but the structures at depth are stable for the set of models. A strong regularization provides very stable models (Fig. 9a) displaying only smooth and large-scale resistivity variations. The patchy surface arising from weak regularizations is more homogeneous in the models obtained from strong regularized inversions.

5.2 Mean resistivity model and stability analysis

In order to reduce inversion-induced noise (section 4.4), as a stacking procedure, and to detect unresolved areas, the mean and the standard deviation of the logarithmic resistivity in the set of inverted field models selected in the previous section are computed on a refined mesh (108 896 cells), on which each inverted model is projected. In the following, the resulting models are respectively referred to as 'mean resistivity model' and 'standard deviation model' (Fig. 10).

The mean resistivity model presents resistivity values in the range [125–2500] Ω m and displays two characteristics:

(1) a strong resistive anomaly located in the first 250 m, below the surface and all over the unstable zone;

(2) a deep conductive area oriented along the north–south direction and located at the east of the unstable zone, with vertical conductive patterns extending from the surface down to this conductive anomaly.

Small size (100 m width) lateral variations are observed at the surface of the model particularly at the location of the resistive anomaly. Such lateral variations are expected to exist at the surface, as attested by the analysis of the two boreholes' core samples (Fig. 1c), and seem to be detected in the mean resistivity model with the stacking procedure. The standard deviation model (Fig. 10) presents values in the range of 6.9×10^{-3} to 2.4×10^{-1} and displays sharp variations mostly at the surface. The maximum values denote small uncertainties of less than 100 per cent in the resistivity value. At depth, the standard deviation model displays values below 1.3×10^{-1}, and does not allow defining the investigation limits of the data set. Even if the resolution is poor at depth, the data still allow determining large-scale variations of the resistivity; these variations are stable from one inverted model to another, but are not interpreted in our analysis.

Locally, the 3-D model is compared with 2-D resistivity profiles of Le Roux *et al.* (2011; Fig. 11). Both the mean resistivity model and the mean model computed from all weakly regularized models (Fig. 9a) are compared with the profiles 3 and 4 from Le Roux *et al.* (2011; Fig. 1b). The two mean models present similar structures along the profiles. The principal difference lies in the resistivity values of the observed structures. The cross-sections from the mean model (Figs 11a and d) display resistivity values of 300–2000 Ω m when the cross-sections from the weakly regularized mean model (Figs 11b and e) display resistivity values reaching 4000 Ω m. This second model approaches closer to the values observed in the profiles from Le Roux *et al.* (2011), showing that, at this location and

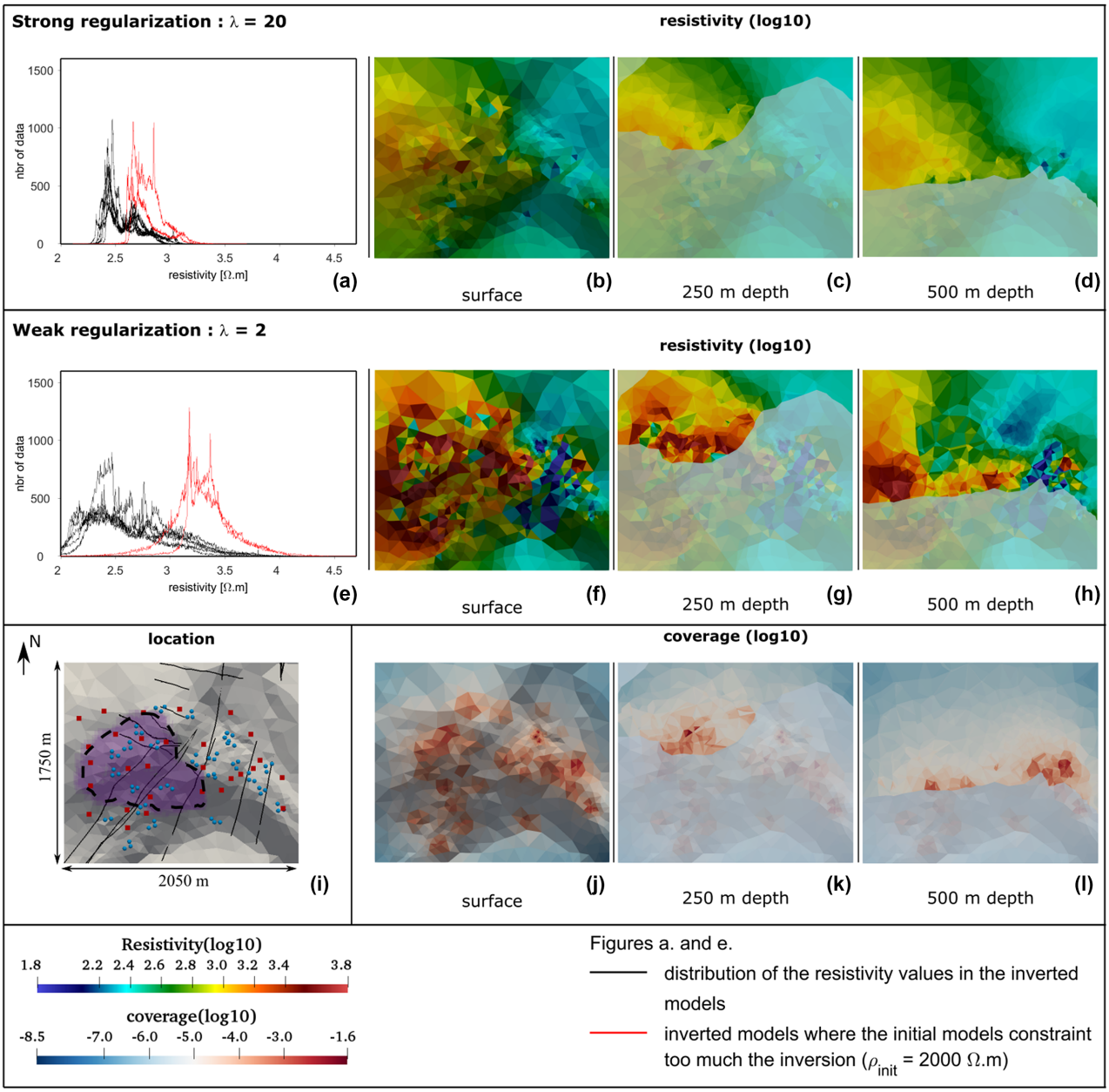

Figure 8. Comparison of the inverted models. First line: inversion results for strong regularizations (LAMBDA = 20): (a) distribution of resistivity values in the set of inverted models (one line corresponds to one inverted model); and an example of inverted model (initial resistivity = 200 Ω m, fine mesh), with the top view (b) and horizontal slices at 250 m depth (the whitened area corresponds to the part of the model where the topography is below the slice) and at 500 m depth. Second line: inversion results for weak regularizations (LAMBDA = 2): (e) distribution of resistivity values in the set of inverted models; an example of inverted model (initial resistivity = 200 Ω m, fine mesh), with the top view (f) and (g) horizontal slices at 250 m depth and (h) at 500 m; (i) location of the major faults (black lines), measurement (blue dotes) and injection (red dots) points and unstable area (purple zone) regarding the inverted model; (j) top view) and (k) horizontal slices at 250 m and (l) 500 m of the data coverage (mean of sensitivity, Günther *et al.* 2006).

at this resolution, the resistivity variations brought by a weak regularization are still data-driven rather than induced by noise. Nevertheless, most of the thin variations contained in the profiles from Le Roux et al. (2011) are not retrieved by the 3-D model, showing the resolution difference between the type of measurements presented in this work and a 2-D profile with an electrode spacing of 5 m. In particular, the profile 3 displays a very conductive anomaly at the east (left-hand side) of the profile reaching the top layers at 50–100 Ω m, which does not appear in the 3-D models. Such an anomaly is observable in the 3-D model, but at much greater depth (around 300 m depth, Fig 13b), suggesting a difference in resolution for the two acquisitions, and a possible difference in hydrological state between the two measurements.

5.3 Interpretability of the geophysical model

Only the patterns that are stable among the set of inverted models are interpreted. Because the mean resistivity model emphasizes

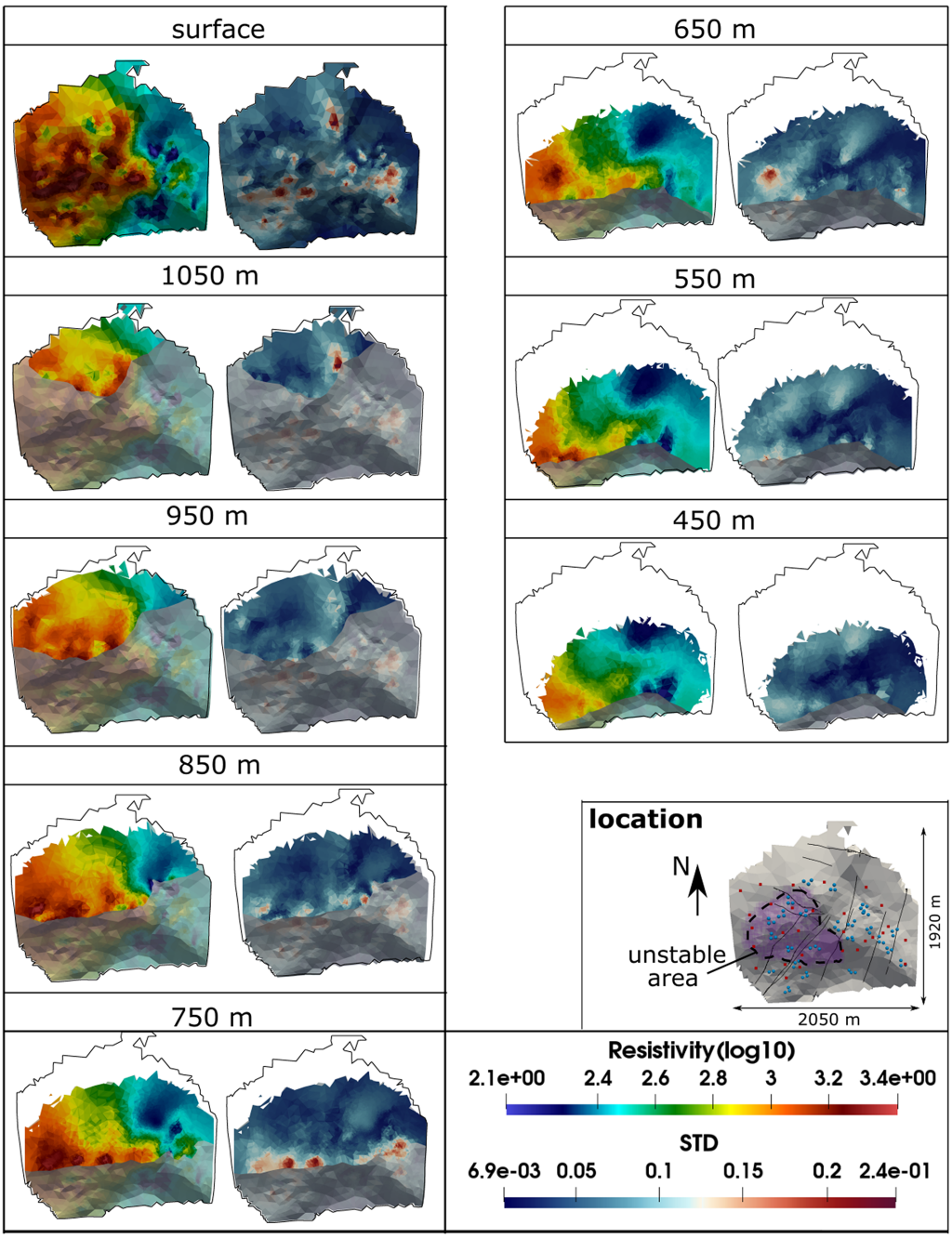

Figure 9. Mean resistivity model and standard deviation model. Horizontal slices at the topographic surface at the elevations 1050, 950, 850, 750, 650, 550, and 450 m (asl).

well these observed patterns, and partly reduces the noise introduced by weakly regularized inversions, it is used as basis for the interpretations proposed in the next section (Figs 8, 10, 12 and 13). The limit of interpretability of a model depends on the size of the object of interest. The data coverage computed during the inversion consists in the sum of the absolute sensitivities. The coverage is used as absolute estimation of sensitivity and a threshold value of 10^{-6} is taken as interpretability limit of the model providing a depth of investigation of around 500 m. This limit is in agreement with the lateral limits of detection inferred from the synthetic tests; however, the synthetic tests also demonstrated that for large anomalies (> 200 m^3), the anomaly could be detected below the depth of investigation defined by the chosen coverage limit, tested up to 1500 m. The synthetic tests indicate that only resistivity variations of more than 20 per cent can be interpreted. Small anomalies (< 200 m^3) located close to the surface are hardly detected. These limitations are caused by the low spatial sampling of the measurements; it forces us to focus on the large-scale anomalies and to address with great care the interpretation of small anomalies observed close to the surface.

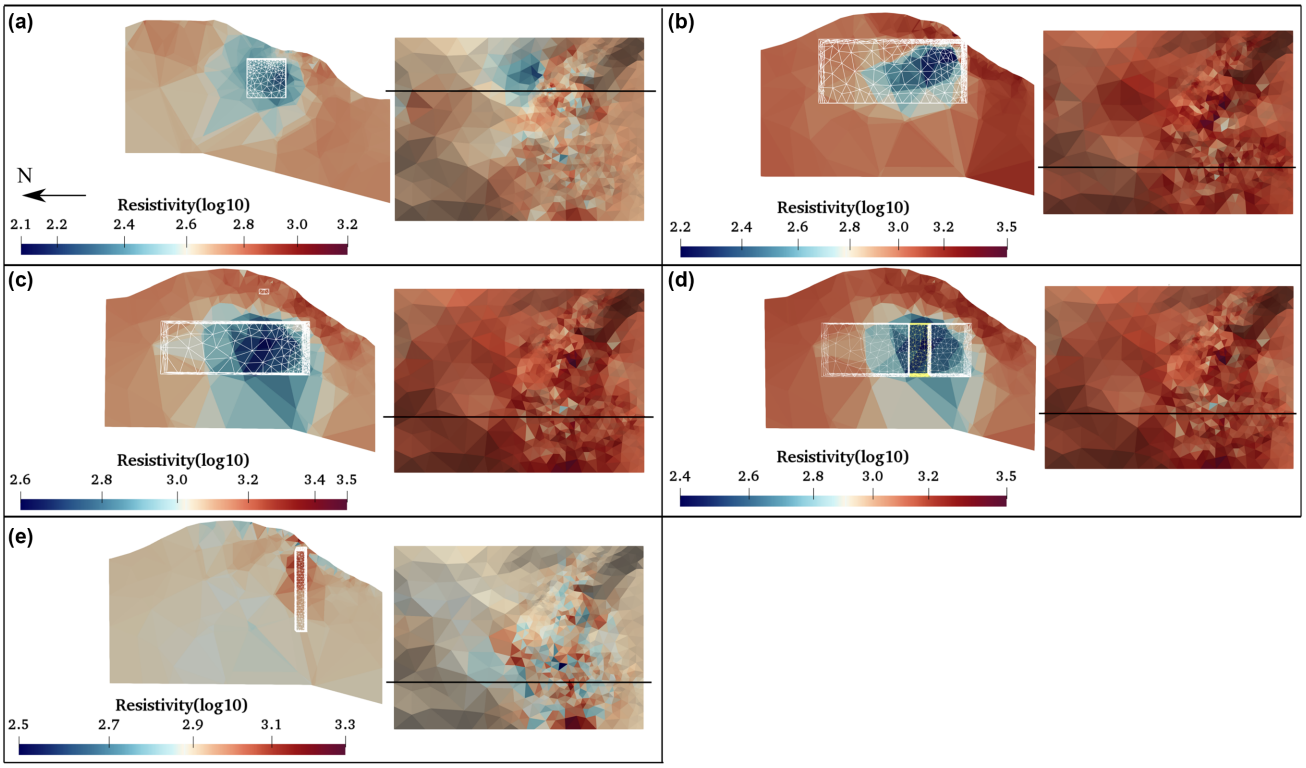

Figure 10. Results of the synthetic tests—exemplary mean inverted models—vertical cross-section and top view—(a) for tests 1–5, (b) tests 6–9, (c) tests 10–12, (d) test 13 and (e) tests 14–16. The cubes delimited by white wireframes are the anomalous bodies.

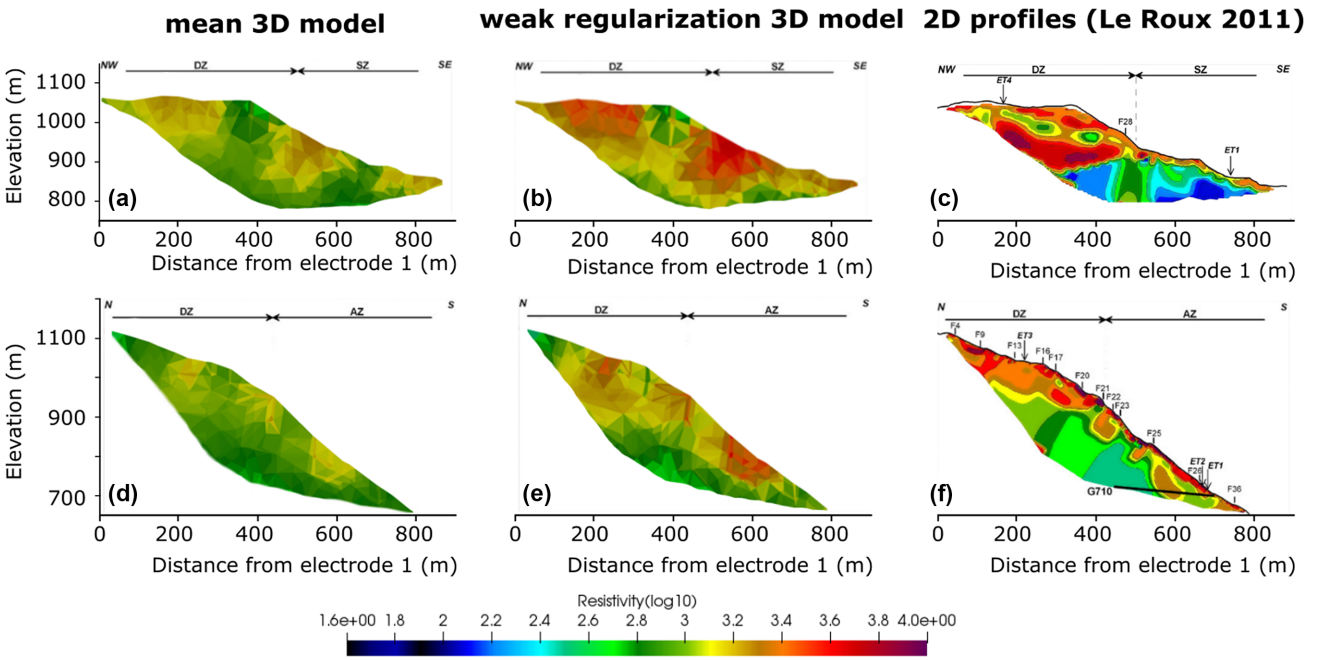

Figure 11. Comparison of the 3-D resistivity models (left and centre) to the 2-D inverted models (right) of Le Roux *et al.* (2011), profiles ET3 and ET4. The 3-D model is sliced at the location of the 2-D investigation profiles. Two 3-D resistivity models are considered: (a and d) the mean resistivity model computed from all stable inverted models, and (b and e) a mean resistivity model computed from all stable models obtained with a weak regularization.

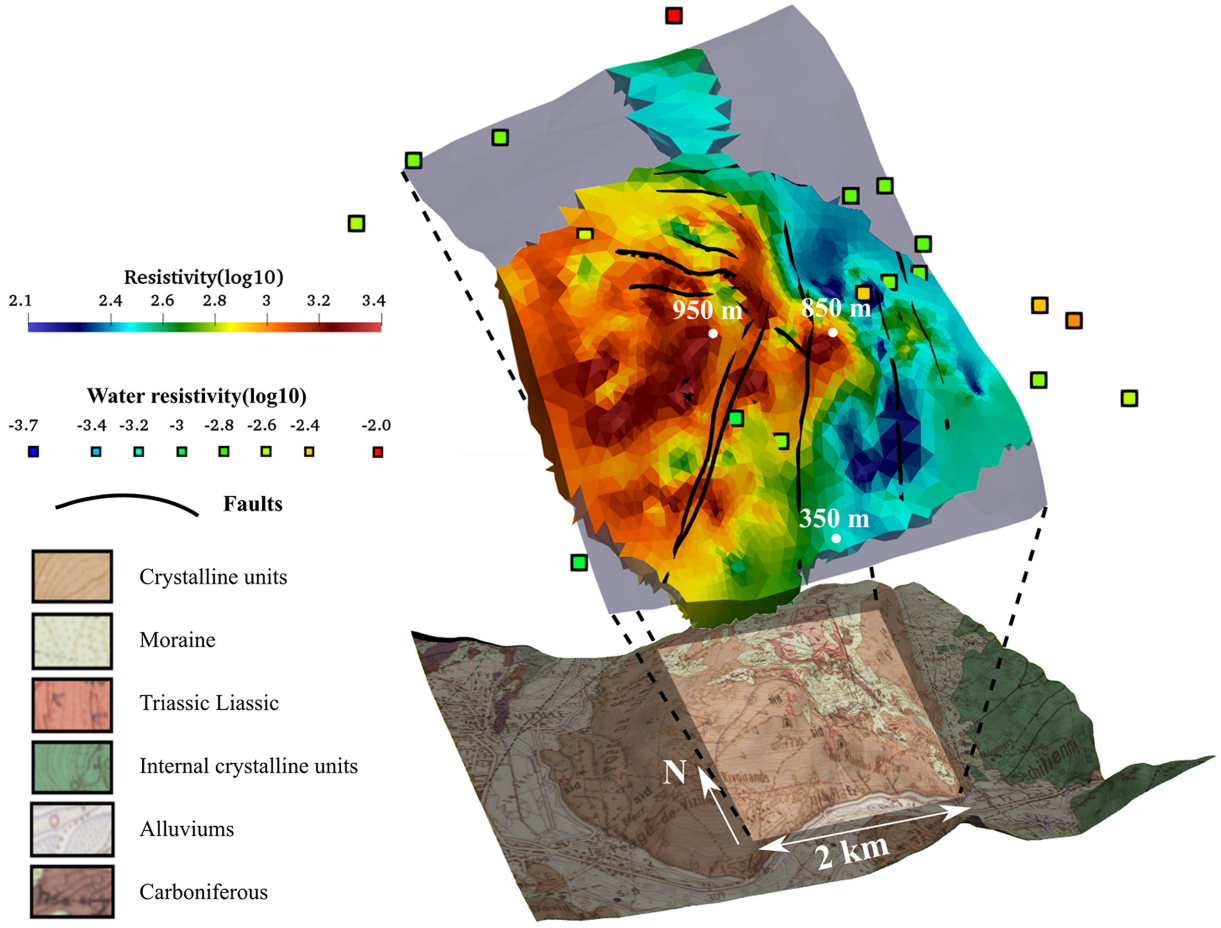

Figure 12. 3-D representation of the interpreted model (mean model computed on the logarithmic resistivity of the set of selected inverted models) superimposed to the geological map of the slope (Barféty *et al.* 1972). The squares represent the resistivity (log10) of the surface waters sampled in spring or at surface runoff locations. The black lines represent the major faults.

6 DISCUSSION: GEOLOGICAL AND HYDROGEOLOGICAL INTERPRETATION OF THE 3-D RESISTIVITY MODEL

Previous geophysical studies (Meric *et al.* 2005; Le Roux *et al.* 2011) identified that variations of electrical and seismic properties correspond quite well with the known delineations of structures controlling the landslide. The variations of geophysical properties are caused by changes in the macrostructure of the slope (geology, fault, crushed area, and fluid chemistry) and microstructure of the media (porosity, veins, composition of the matrix, and presence of clays). In particular, the highest resistivity values are detected at locations where the rock is densely fractured and damaged (Le Roux *et al.* 2011). The variations of geophysical properties are also caused by water circulation and more specifically changes in the water flow regime in zones with high clay contents as identified by self-potential measurements (Meric *et al*. 2005). The zones of lowest resistivity values correspond to the location of permanent ground water in the fractures and of high clay content. The anomalies observed in the 3-D mean resistivity model are interpreted with complementary information (borehole core samples, fault model and water chemistry).

6.1 Identification of geological and geomorphological structures

The strong resistive anomaly in the Western sector of the model is presented in the Figs 13(a) and (b). The anomaly is interpreted by Le Roux *et al.* (2011) as a very fractured and dry material. We expand this interpretation, suggesting, from a hydrological perspective, that the degree of fracturation in this zone makes it very permeable; this is confirmed by the absence of water sources in most of this area. The boundary at depth of this resistive anomaly can be interpreted in two ways. A decrease of the electrical resistivity with depth could correspond either to a transition to a more compact and less damaged micaschist, or to the transition from a dry to a water saturated material. The resistivity transition is located at an altitude of about 500–600 m, which is the known altitude of the deep aquifer. It seems therefore that the resistivity limit of 500 Ω m corresponds to the bottom of the vadose zone. At the surface, the high resistivity patches (2500 Ω m) align along the major faults (Fig. 12). This observation suggests that the degree of fracturation close to the surface (50–200 m depending on the location) is inhomogeneous. It is possible to delineate the most damaged areas, which extend laterally from the fault planes, up to a distance of 100 m, to a less damaged material, presenting a resistivity below 1500 Ω m. At depth (100–250 m), these trends seem to vanish as the resistivity

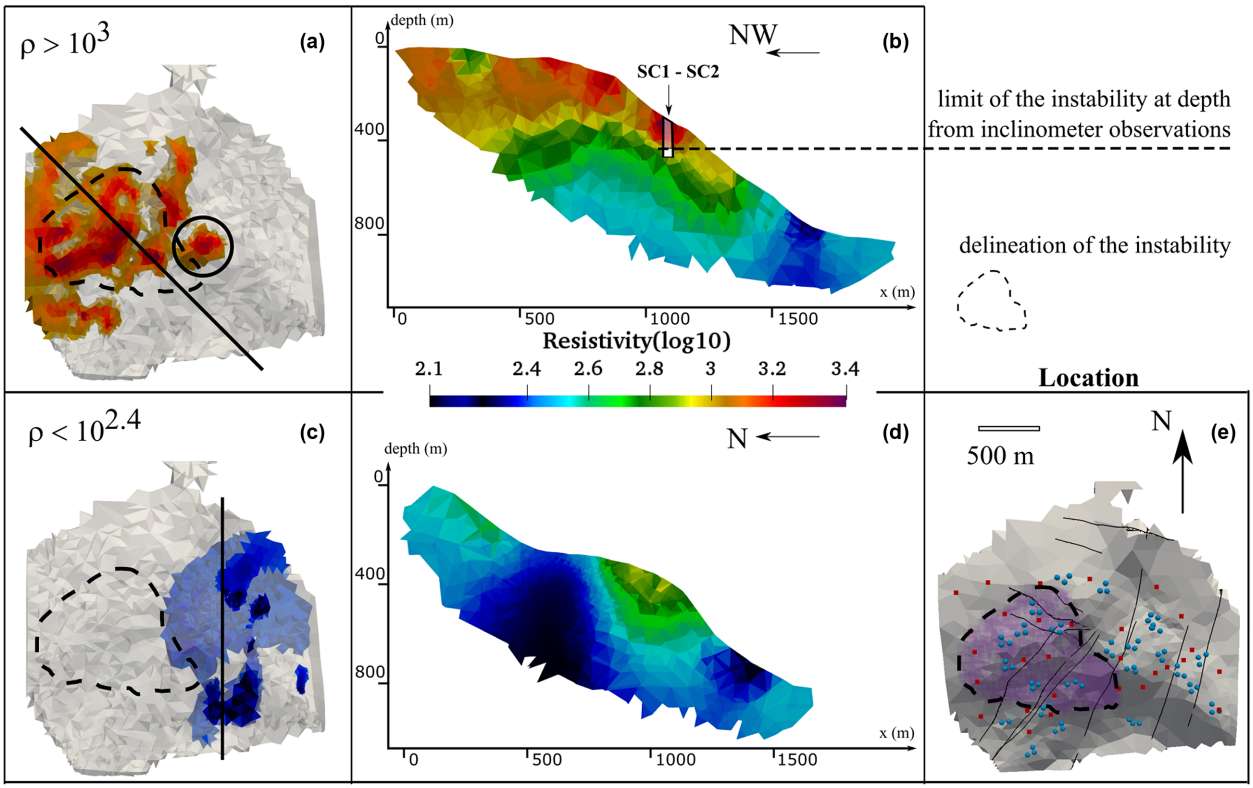

Figure 13. Resistive and conductive anomalies observed at the Séchilienne slope. (a) Top view of the extracted resistivity anomaly (resistivity above 10^3 Ω m), the black line is the location of the cross-section in (b) and the black circle is the part of the resistive anomaly located outside of the unstable area. (b) Vertical cross-section of the mean resistivity model showing the transition at depth from the resistive anomaly to the more conductive background. (c) Top view of the extracted conductive anomaly (resistivity below $10^{2.4}$ Ω m, i.e. 250 Ω m), the black line is the location of the cross-section in (d). (d) Vertical cross-section of the mean resistivity model showing the conductive vertical patterns expanding from the surface down to a major deep conductive anomaly. (e) Acquisition setup: injection points in red and potential electrodes in blue, the unstable area is highlighted in purple.

drops. Because of the low resolution and the loss of detectability at depth, it is not possible to estimate the dip of the observed faults.

The inclinometer observations indicate a limit of the instability at a depth of 110 m below the surface. Assuming that the resistivity variations are directly and only correlated to the structural properties of the material at this depth and can be therefore an indicator of the geomechanical behaviour, resistivity values above 1000 Ω m could be attributed to unstable mass.

From the observation of this very resistive zone, two remarks can be made:

(1) From a geophysical and geomechanical point of view, the highly resistive zones should be specific to the unstable area (active zone); however, high resistivity values are also noticeable outside of the unstable area (Fig. 13a, see the area circled in black). The high resistivity values observed in this area certainly correspond to a highly damaged zone, and it is unclear why this zone has not currently experienced high displacement rates (Chanut *et al.* 2013).

(2) The active zone of 'Les Ruines', which is the zone experiencing the highest displacement rates, does not appear as very resistive. Its resistivity is of about 1000 Ω m, while the maximum observed resistivity is of about 2500 Ω m close to the fault planes. In the location of les Ruines, it seems that the topography and the fault segmenting the slope above this zone play a major role in the observed toppling movement.

6.2 Identification of hydrological structures

The deep conductive anomaly in the Eastern sector of the model is presented in Figs 13(c) and (d). The main part of the anomaly is a slope-scale conductive trend oriented along the north/south structure of the Sabot fault, with resistivity values ranging from 125 to 250 Ω m. Synthetic tests showed that large cubic resistive anomalies located in this area always have underevaluated conductivities in the inverted models; it is therefore expected that the resistivity values obtained for this anomaly are overestimated.

Vertical thin conductive anomalies locally extend from the surface down to the deep conductive anomaly. These vertical patterns present similar resistivity values as the main conductive anomaly. They could be discussed as the synthetic tests showed that a parallelepiped conductive anomaly at the location of the large north–south anomaly could produce, through the inversion process, a spread of the anomaly towards the surface, producing the same types of patterns as the ones observed in the inverted models. We however believe that these patterns exist, because they represent a strong anomaly, with resistivity values as low as the rest of the conductive anomaly. In the synthetic tests, the spread patterns present smaller conductivity values than the conductive anomaly producing it.

The abundance of water outflows in this area suggests a wet rock, and the possibility that water can be stored in the near-surface rock. These outflows are largely sampled and documented in a geochemical monitoring of the slope (Mudry and Etievant 2007;

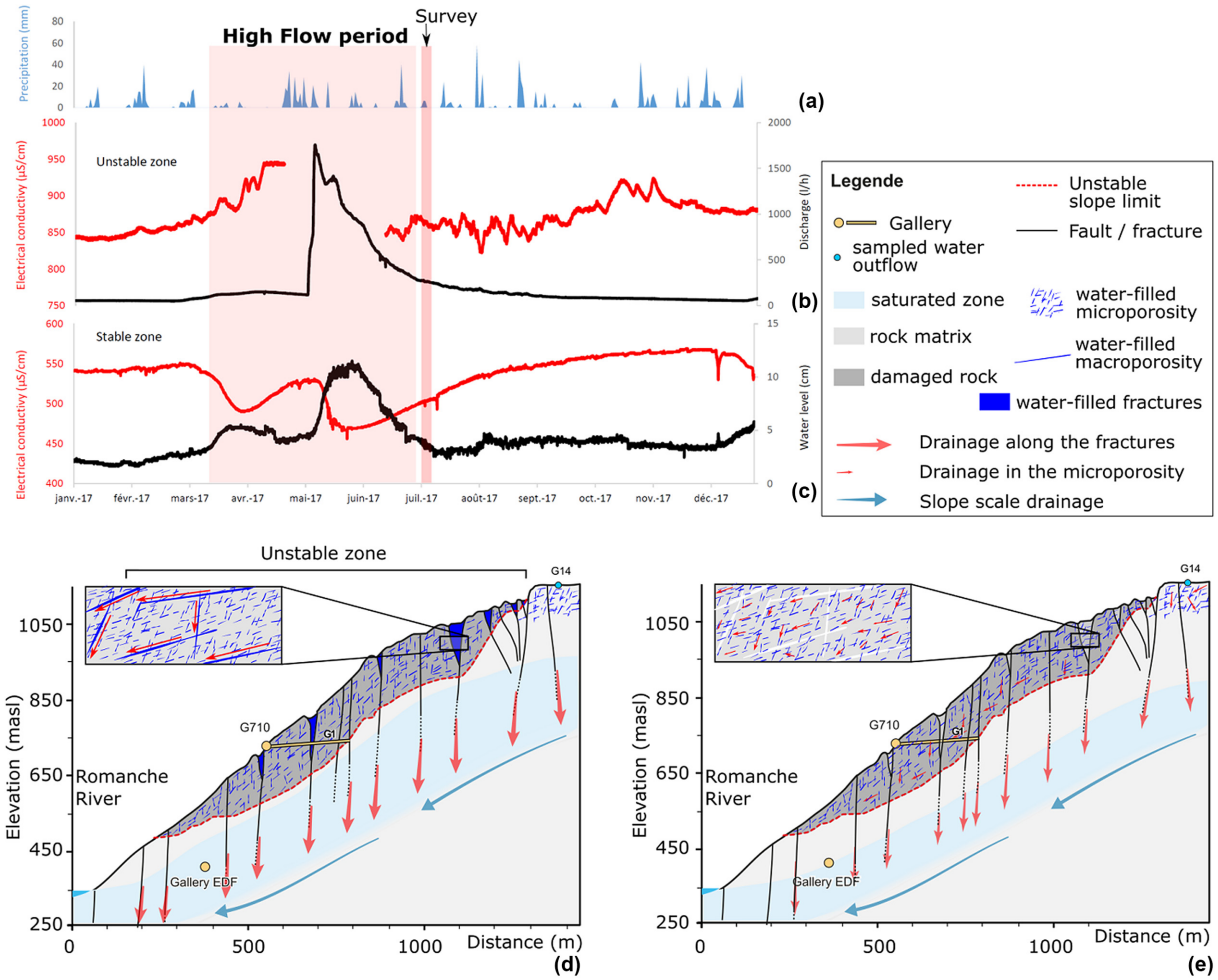

Figure 14. Hydrogeological measurements during the year 2017 and hydrogeological concept. (a) Yearly precipitation recorded at Mont Sec. (b) Water electrical conductivity and discharge in the unstable zone, recorded at the G710 gallery. (c) Electrical conductivity and water level recorded in the stable zone. Hydrogeological conceptual model of the Séchilienne slope for periods of (d) high flow and (e) low flow (modified from Vallet *et al.* 2015).

Vallet *et al.* 2015). Vallet *et al.* (2015) described this area as a major drain of the massif, and concluded, from the analysis of water chemistry, that water coming from the west and the north of the fault cluster along the Sabot fault, at the location of the conductive anomaly.

In relation to the hydrological observations (Fig. 14), we interpret these conductive anomalies in the stable area as local perched aquifers discharging downwards in the main aquifer. These perched aquifers develop during high water periods, favoured by the permeability contrasts between decompressed zones of increased porosity located at the surface, and the unaltered rock. The Sabot fault acts as a drain, easing the water transfers from the perched aquifer to the main aquifer. At the end of the high waters period, the perched aquifers—constantly supplied during high-flow periods by rainfall—progressively discharge in the main aquifer drained by the Sabot fault. Throughout the low-flow period, this process applies at first to the water located in the largest pores and concerns, at the end of the low-flow period, the water located in the micropores.

During the high-flow periods, the water level of the deep aquifer is directly controlled by the precipitation and the rapid infiltration, while in low-flow periods, the flow is maintained by the restitution of the water stored in the rock microporosity. The microporosity is characterized by an important capacitive function and the water presents an increased mineralization, due to its increased residence time in the rock. The joint analysis of the variation in water level and the variation of electrical conductivity (Fig. 14c) illustrates the importance of the drainage of the microfissured matrix during the low-flow period, at which the increase in water conductivity is the direct consequence of the discharge of the water from the microfissures.

The 3-D ERT survey has been conducted in 2017 July at the start of the low-flow period. At that moment, the perched aquifers are still maintained by the presence of water contained in the small-sized pores, while the water from the largest porosity has already been drained out towards the deep aquifer.

In the unstable zone, a dense network of opened fractures (as illustrated in Fig. 1c) allows rapid groundwater flows along these preferential flow paths. In low-flow periods, similar processes as the ones described before for the stable area occur, and the water flow towards the saturated zone is enabled by the restitution of the water stored for several months in the microporosity of the matrix. The volume of water involved in this process is however smaller than in the stable area (the discharge is close to 0 L h^{-1} in most of the

low-flow period, Fig. 14b) highlighting a smaller storage capacity as in the stable zone.

7 CONCLUSIONS AND PERSPECTIVES

The use of the novel R-DAS FullWaver has proven successful to infer new knowledge on the large-scale geological and hydrogeological structures of the Séchilienne slope. The scale of the study, together with the sparse and uneven sampling are uncommon in the spectrum of resistivity surveys, where a regular sampling provides sensitivity variations which are easy to capture and understand. This unusual layout led us to carry an extensive analysis of the sensitivity in order to understand the ability of our data set to detect specific anomalies, including an analysis of the stability of the inverted models, and the realization of synthetic tests. The analysis of stability highlighted the unresolved mesh located at the surface of the model; the synthetic tests allowed identifying the main anomalies observed in the inverted models. These tests provided some remarkable results.

(1) First, despite the minimal electrode distances of 50 m, the data set seemed not to be sensitive to small-scale anomalies close to the surface (< 200 m^3).

(2) Second, the sparse layout and the strong topography variations are prompt to produce artefacts in the inverted model;

(3) Third, large-scale anomalies (> 200 m^3) are always detected in the sensitive zone of the models.

(4) Fourth, the sensitive zone is defined by a threshold in the coverage value (10^{-6}), providing a depth of investigation of 500 m. Large-scale anomalies are also detectable at greater depths within the simple contexts simulated in the synthetic tests (e.g. the inversion was sensitive to the bottom of an anomaly located at 1500 m depth).

(5) Fifth, the resistivity values of the detected anomalies are not correctly retrieved in the inverted model. According to the synthetic tests, anomalies seem to be underestimated.

The unstable zone has been detected in the model as a resistive anomaly (with resistivity values $> 1500\ \Omega$ m) where the damage is mostly located along the major faults crossing the Mont Sec slope, until a distance of about 100 m. A large conductive anomaly at the east of the landslide (Sabot fault) is detected and interpreted as a perched aquifer. At the end of the high-flow period, when the geophysical survey was realized, these remaining perched aquifers correspond to water stored in the micro-porosity, discharging in the deep aquifer. These interpretations are in very good accordance with the hydrogeological understanding arising from hydrochemical observations, and could be fully confirmed by repeating this analysis with measurements realized during the high-flow period.

The main limitations of the work are the local poor spatial sampling. A major improvement could be to increase the number of receivers in order to densify the spatial sampling. The detectability of smaller scale anomalies close to the surface would thus be increased. However, adding a few receivers would increase a lot the duration and effort needed for the survey, and given the rough topography and the difficulty to access the most damaged locations, some areas would necessarily remain uncovered. The presented methodology is applicable to similar contexts where the large scale geological and hydrogeological features of a site are questioned. A regular sampling, as dense and regular as possible should be considered, and sensitivity tests should also be carried out, as they have proven to be very insightful to capture the sensitivity of an inverted data set.

ACKNOWLEDGEMENTS

This work is part of the French Landslide Observatory OMIV (Observatoire Multi-disciplinaire des Instabilités de Versants—ano-omiv.cnrs.fr) and has been financially supported by the project HYDROSLIDE (High frequency hydrogeophysical observations for a better understanding of landslides mechanical behaviour, ANR-15-CE04-0009) and the project CRITEX (Challenging equipment for the spatial and temporal exploration of the critical zone, ANR-11-EQPX-0011) both funded by the French Research Agency (ANR). The authors would like to thank Pierrick Bornemann, Anne Puissant, Orlando Leite, Kusnahadi Susanto, Sophia Laporte, Pauline Rousson, Fabrice Vermeersch and Stéphanie Moriset for their help in the field. We further thank Thomas Günther (LIAG, Hanover) for helpful discussions on the use of the inversion and modelling software BERT, as well as the two anonymous reviewers who helped improving the clarity of the manuscript.

REFERENCES

Alfonsi, P., 1997. Relation entre les paramètres hydrologiques et la vitesse dans les glissements de terrains. Exemples de La Clapière et de Séchilienne (France), *Rev. Fr. Géotech.,* **79,** 3–12.

Barféty, J.C., Bordet, P., Carme, F., Debelmas, J., Meloux, M., Montjuvent, G., Mouterde, R. & et Sarrot Reynauld, J., 1972. Carte geologique détaillée de la France (1/50000) n° 797 Vizille, *Editions du BRGM,* p. 38, Orléans (France).

Baudement, C., Bertrand, C., Guglielmi, Y., Viseur, S. & Vallet, A., 2013. Quantification de la dégradation mécanique et chimique d'un versant instable: approche géologique, hydromécanique et hydrochimique Etude du versant instable de Séchilienne, Isère (38), in *JAG2013,* 3èmes Journées Aléas Gravitaires, Strasbourg, France, pp. 1–6.

Cappa, F., Guglielmi, Y., Viseur, S. & Garambois, S., 2014. Deep fluids can facilitate rupture of slow-moving giant landslides as a result of stress transfer and frictional weakening, *Geophys. Res. Lett.,* **41**(1), 61–66.

Chanut, M.A., Dubois, L., Duranthon, J.P. & Durville, J.L., 2013. Mouvement de versant de Séchilienne : relations entre précipitations et déplacements, *Rev. Fr. Géotech.,* **79,** 3–12.

Dubois, L., Chanut, M.A. & Duranthon, J.P., 2014. Amélioration continue des dispositifs d'auscultation et de surveillance intégrés dans le suivi du versant instable des Ruines de Séchilienne, *Géologues,* **182,** 50–55.

Duranthon, J.P., Chanut, M.A. & Dubois, L., 2013. Ruines de Séchilienne, rapport annuel de suivi du site, avril 2012 (mars 2013), CETE - Centre d'Etudes Techniques de LYON, **41829-1,** p. 119.

Duranthon, J.P. & Effendiantz, L., 2004. Le versant instable des "Ruines" de Séchilienne: point sur l' activité du phénomène et présentation du nouveau dispositif de gestion de la télésurveillance, *Assoc. Fr. Topogr.,* **252,** 29–48.

Duranthon, J.P., Effendiantz, L., Memier, M. & Previtali, I., 2003. Apport des méthodes topographiques et topométriques au suivi du versant rocheux instable des ruines de Séchilienne, *XYZ - Association Française de Topographie,* **94,** 31–38.

Fox, R.C., Hohmann, G.W., Killpack, T.J. & Rijo, L., 1980. Topographic effects in resistivity and induced-polarization surveys, *Geophysics,* **45**(1), 75–93.

Friedel, S., Thielen, A. & Springman, S.M., 2006. Investigation of a slope endangered by rainfall-induced landslides using 3D resistivity tomography and geotechnical testing, *J. appl. Geophys.,* **60,** 100–114.

Gance, J., Sailhac, P. & Malet, J.P., 2015. Corrections of surface fissure effect on apparent resistivity measurements, *Geophys. J Int.,* **200(2)**, 1118–1135.

Guglielmi, Y., Vengeon, J., Bertrand, C., Mudry, J., Follacci, J. & Giraud, A., 2002. Hydrogeochemistry: an investigation tool to evaluate infiltration into large moving rock masses (case study of La Clapière and Séchilienne alpine landslides), *Bull. Eng. Geol. Environ.,* **61**(4), 311–324.

Günther, T., Rücker, C. & Spitzer, K., 2006. Three-dimensional modelling and inversion of DC resistivity data incorporating topography–II. Inversion, *Geophys. J. Int.,* **166**(2), 506–517.

Helmstetter, A. & Garambois, S., 2010. Seismic monitoring of Séchilienne rockslide (French Alps): analysis of seismic signals and their correlation with rainfalls, *J. geophys. Res.,* **115,** F03016, doi:10.1029/2009JF001532.

Jongmans, D. & Garambois, S., 2007. Geophysical investigation of landslides: a review, *Bull. Soc. Géol.,* **178**(2), 101–112.

Legchenko, A., Clément, R., Garambois, S., Maury, E., Mic, L.M., Laurent, J.P., Desplanque, C. & Guyard, H., 2011. Investigating water distribution in the Luitel Lake peat bog using MRS, ERT and GPR, *Near Surf. Geophys.,* **9**(2), 201–209.

Le Roux, O., Jongmans, D., Kasperski, J., Schwartz, S., Potherat, P., Lebrouc, V., Lagabrielle, R. & Meric, O., 2011. Deep geophysical investigation of the large Séchilienne landslide (Western Alps, France) and calibration with geological data, *Eng. Geol.,* **120**(1), 18–31.

Meric, O., Garambois, S., Jongmans, D., Wathelet, M., Chatelain, J.L. & Vengeon, J., 2005. Application of geophysical methods for the investigation of the large gravitational mass movement of Séchilienne, France, *Can. Geotech. J.,* **42(4)**, 1105–1115.

Montjuvent, G. & Winistorfer, J., 1980. Glaciations quaternaires dans les Alpes franco-suisses et leur piedmont, *Géol. Alpine,* **56,** 251–282.

Mudry, J. & Etievant, K., 2007. Synthèse hydrogéologique du versant instable des Ruines de Séchilienne, *UMR Chrono-Environnement, University of Franche-Comté, Besançon,* **45,** Unpublished Report.

Rochet, L., Giraud, A., Antoine, P. & Evrard, H., 1994. La déformation du versant sud du Mont-Sec dans le secteur des ruines de Séchilienne (Isère), *Bull. Int. Assoc. Eng. Geol.,* **50**(1), 75–87.

Rücker, C., Günther, T. & Spitzer, K., 2006. Three-dimensional modelling and inversion of DC resistivity data incorporating topography–I. Modelling, *Geophys. J. Int.,* **166**(2), 495–505.

Travelletti, J. & Malet, J.P., 2012. Characterization of the 3D geometry of flow-like landslides: a methodology based on the integration of heterogeneous multi-source data, *Eng. Geol.,* **128,** 30–48.

Uhlemann, S., Wilkinson, P., Chambers, J., Maurer, H., Merritt, A., Gunn, D. & Meldrum, P., 2015. Interpolation of landslide movements to improve the accuracy of 4D geoelectrical monitoring, *J. appl. Geophys.,* **121,** 93–105.

Uhlemann, S. *et al.*, 2017. Four-dimensional imaging of moisture dynamics during landslide reactivation, *J. geophys. Res.,* **122**(1), 398–418(Earth Surface).

Vallet, A., Bertrand, C., Mudry, J., Bogaard, T., Fabbri, O., Baudement, C. & Régent, B., 2015. Contribution of time-related environmental tracing combined with tracer tests for characterization of a groundwater conceptual model: a case study at the Séchilienne landslide, western Alps (France), *Hydrogeol. J.,* **23**(8), 1761–1779.

Vallet, A., Charlier, J.B., Fabbri, O., Bertrand, C., Carry, N. & Mudry, J., 2016. Functioning and precipitation-displacement modelling of rainfall-induced deep-seated landslides subject to creep deformation, *Landslides,* **13**(4), 653–670.

Vengeon, J.M., 1998. Déformation et rupture des versants en terrain métamorphique anisotrope. Apport de l' étude des Ruines de Séchilienne, *PhD thesis*, Université Joseph-Fourier-Grenoble I, p. 185.